Space Science Reviews (2022) 218:61
https://doi.org/10.1007/s11214-022-00928-w

Time Delay Integration Imaging of the Nighttime Ionosphere from the ICON Observatory

S.B. Mende[1] · H.U. Frey[1] · S.L. England[2] · T.J. Immel[1] · R.W. Eastes[3]

Received: 30 May 2022 / Accepted: 7 October 2022 / Published online: 27 October 2022

Abstract
One of the objectives of the Far UltraViolet (FUV) imager on the Ionospheric Connection Explorer (ICON) spacecraft is to make high resolution images of the nighttime near equatorial oxygen 135.6 nm airglow emission. This emission is largely the product of O^+ ion re-combination and therefore the emission intensity is a proxy for remote measurement of ionospheric density. The ICON FUV instrument is capable of high resolution imaging of the night glow by viewing the Earth's limb from above on the left side of the spacecraft and taking rapid exposures and co-adding the resultant images for 12 seconds. To improve the resolution and compress the resulting data a new type of Time Delay Integration (TDI) technique was developed, which involves transforming the images into a distorted frame so that the displacement due to orbital motion becomes a singular constant vector for all pixels. Operating in this transformed frame it is possible to co-add and shift the images to retain the resolution and minimize the required data bandwidth. The transformation needs modeling of the object distance for all pixels. Two models, the "limb" and "sub-limb" models, are used for transforming the upper and lower parts of the ICON FUV images, respectively. At the input of the instrument there is a rotatable mirror, which allows directing the optic axis near to the plane of the local magnetic field. The images are co-added for 12 sec and are down linked and re-assembled on the ground into maps of the O emission showing an entire night pass. This is the first report on the performance of this newly developed TDI system. ICON with its low inclination (27 degree) orbit provides an extensive longitudinal coverage on each orbit complementing the coverage of GOLD or TIMED. During 179 orbits in October 2021 ICON FUV saw significant nighttime ion densities on 76% of the orbits. At low latitudes the ionization was clearly associated with the equatorial ionospheric anomaly (EIA). The maps showed significant structuring during 34% of the orbits when ICON was in the position to view the EIA. In coordinated observations GOLD and ICON FUV observed regular structuring in the form of Equatorial Plasma Bubbles (EPB-s). Comparing to GOLD observations in 2018, ICON saw significantly fewer EPB-s in the month of October 2021. ICON TDI integrated sub-limb view was tested for resolution using star images and should have seen structures less than 10 km. From the 179 orbits taken in October 2021 the shortest repetition EPB-were 350 km from peak to peaks.

Keywords Imaging the ionosphere · Ultraviolet imaging · Equatorial ionosphere · Frequency of equatorial plasma bubbles

The Ionospheric Connection Explorer (ICON) Mission: First Results
Edited by David E. Siskind, Ruth S. Lieberman and Jeffrey Klenzing

Extended author information available on the last page of the article

1 Introduction

One of the main objectives of the far-ultraviolet (FUV) imager on the ICON spacecraft is to make nighttime images of the near equatorial oxygen 135.6 nm airglow. The nighttime Far Ultra Violet (FUV) OI 135.6-nm emission is produced mostly by recombination of O^+ oxygen ions. O^+ can recombine directly with electrons to form O atoms or undergo ion-ion mutual neutralization ($O^- + O^+$). Although both processes produce OI 135.6-nm emission at all local times, this emission is most observable on the nightside where no competing dayglow is present. The nighttime emission can be used to sense O^+ recombination processes remotely. At low latitudes near the equator the emission is most intense in the equatorial ionization anomaly (EIA) (Appleton 1946). Strong FUV emissions near the equator from the ionosphere were discovered by photometers on the OGO-5 satellite (Hicks and Chubb 1970). In the equatorial region during the day and early evening the dynamo electric field and magnetic field produce an $\mathbf{E} \times \mathbf{B}$ force that moves the F-region plasma to higher altitudes and latitudes. The plasma transport perpendicular to B leaves less dense ionization near the magnetic equator at the lower altitudes. The result is the formation of two belts of high ionization density at around magnetic dip latitudes of 15°N and 15°S. These are the crests of the equatorial ionization anomaly (EIA) (Appleton 1946; Hanson and Moffett 1966). The enhanced ion concentrations are seen as two bands near the equator, each typically centered near $\pm 15°$ magnetic latitude during geomagnetically quiet conditions, however they are generally quite variable (Immel et al. 2009). There are also variations due to the tilt, offset, distortion of the Earth's magnetic field and atmospheric tides (e.g., Immel et al. 2006; Lühr et al. 2007). During magnetic storms other effects can be significant such as penetration electric fields and neutral wind disturbances that can disrupt the usual morphology

The 135.6 nm FUV emissions can be used to observe the climatology of the nightside ion density in the EIA. With the exception of the polar aurora, the emission from the EIA is brighter than most other forms of 135.6 night airglow and it is approximately ten times dimmer than the daytime 135.6 nm glow which is directly excited by solar excited photoelectrons. The FUV instrument on the IMAGE mission (Mende, 2000) was able to capture broader morphology of the FUV emission for multiple hours when the IMAGE satellite apogee was at low latitude (Immel et al. 2006). The Global Ultra Violet Imager (GUVI) on the TIMED satellite observed the EIA regularly. In general the EIA northern and southern branches are well separated but at times the two branches come together. Basu et al. (2009) found a relationship between the branches coming together and the formation of an equatorial counter electrojet.

Equatorial Plasma Bubbles (EPB-s) can be seen as modulations of the intensity of the nighttime 135.6 nm emission from the EIA. EPB-s are believed to be generated by the generalized Rayleigh-Taylor instability (RTI) (Balsley et al. 1972; Haerendel 1974; Ossakow 1981; Sultan 1996; Woodman and La Hoz 1976) with varying degree of contributions of background ionospheric/thermospheric parameters, height and gradient of the bottom side F layer, electric field, wind, conductivity, and spatial perturbation in the electron density at the bottom of the F region as a seed.

At sunset, the F-region conductivity gradient caused by the sunset terminator and zonal neutral wind produce an enhanced eastward electric field on the dayside of the terminator and a westward electric field on the nightside (Rishbeth 1981; Farley et al. 1986; Eccles 1998). The enhanced eastward electric field, called the pre-reversal enhancement (PRE), lifts the F region. If the PRE is large enough, then it can steepen the bottom side of the F region increasing the probability of producing an instability such as the Rayleigh-Taylor (RT) instability. In the presence of a steep gradient gravity waves or other ionospheric perturbation has a high probability of initiating a RT instability. As a result, plasma inhomogeneities

or bubbles can form (Ossakow 1981), and these irregularities theoretically can range from hundreds of kilometers to tens of centimeters in size. The PRE and the resultant eastward electric field has an important role in destabilizing the ionosphere creating irregularities and producing scintillation of radio-frequency signals (Basu et al. 1996; Fejer et al. 1999).

Equatorial plasma bubbles (EPB-s) have horizontal spacings of 100-800 km. (Kelley et al. 1981 (spacing = 600-700); Makela et al. 2010 (spacing = 100-500); Makela and Otsuka 2012 (spacing=100-600); Röttger 1973 (spacing 210-640); Singh et al. 1997 (spacing = 150-800); Takahashi et al. 2009 (spacing = 100-300); Tsunoda and White 1981 (spacing = 400), Hysell and Chau 2006 (spacing∼200)).

Das et al. (2021) performed detailed analysis to find out under what ionospheric conditions the background produced growth of the Rayleigh Taylor Instability (RTI) result in EPB-s. Their analysis suggested that the day to day variability in EPB development is governed by large scale wave structures (LSWS). The LSWS minima in electron density are the sites for the EPB development. LSWS with horizontal wavelength of 200-660 km act as seed for the growth of the RTI. Martinis et al. (2021) investigated EPB climatology in the GOLD images and compared them with the Rayleigh-Taylor instability theory to observe the dependence of bubble growth rate on the direction of the geomagnetic field. Their result suggests that Tsunoda's hypothesis of having the solar terminator and B field aligned is a factor for increasing EPB growth rates (Tsunoda 1985).

The GOLD experiment launched into geosynchronous orbit at 47.5°W geographic longitude provides relatively high cadence, synoptic views of the EIA FUV emissions (Eastes et al. 2020). Eastes et al. (2019) found that intensification of the EPB-s in GOLD images is usually accompanied by the increase of the distance between the north south crests of the EIA. Cai et al. (2020) compared GOLD images with TEC measurements and found good agreement between image brightness and TEC.

Ground-based observations also can provide high temporal coverage and fine spatial resolution images of the EPB-s in visible OI 630 nm or near IR 777.4 nm emissions (Makela et al. 2010; Takahashi et al. 2015) but the spatial coverage ground based observations is limited.

In our work we use the ICON FUV instrument as a two dimensional monochromatic imager with the Time Delay Integration (TDI) technique. The definition of time delay integration in Wikipedia usually refers to a charge-coupled device (CCD) which is used as an image sensor for capturing images of moving objects at low light levels and it works by synchronized mechanical and electronical scanning, so that the image motion is compensated and dim images on the sensor can be integrated over longer periods of time. The ICON FUV instrument has a UV to visible converter intensifier which is followed by a CCD that records individual light pulses produced by the intensifier. Instead of shifting the whole image as in conventional CCD systems our TDI system loads the image into memory at a fast frame rate and by dynamically modifying the addresses of the pixels, the image is shifted in a synchronized manner to remove the motion of the object.

The optical system allows viewing in a direction approximately perpendicular to the orbit track on the left side of the S/C. The S/C motion would generate a horizontal smear of the image and the TDI technique is used to eliminate this smear and improve the overall spatial resolution. The imager takes 100 exposures which are summed into a single image on board using the TDI technique and then sent to ground.

On the ground, a sequence of these images can be used to construct a snapshot geographic map image of the night side ionospheric luminosity on one side of ICON's orbit. As a preliminary analysis we processed all orbits of ICON TDI data every third day for one month, October 2021. We examined the day to day variation of the FUV snapshot images.

Since each day provided approximately 15 orbits we had data for 179 orbits. The orbits were categorized according to the content of the images from no observed nightglow to diffuse glow, to glow with structures, to glow with field aligned depletions, and to sequences of field aligned bubbles. The relative frequency of occurrence of bubbles were compared to bubble counting statistics of GOLD. GOLD obtains medium resolution images of bubbles at one fixed geographic longitude location whereas ICON takes images of bubbles globally at all longitudes. GOLD has the advantage of being able to stare at the bubbles and get information on the temporal nature of bubble development since it is located at a fixed geostationary point above the earth unlike ICON, which produces single snapshots but at varying geographic locations. Due to the TDI technique and ICON's proximity to the atmosphere ICON FUV should have much higher spatial resolution.

The programmed steering of the turret was implemented in the summer of 2021 and there is not yet a complete set of data for all 4 seasons. This paper demonstrates the technique and the instrument performance to make climatological measurements about the bubble statistics when the complete year's data will be available. This is the first report on the performance of the novel TDI system which was developed for the ICON mission

1.1 The ICON Data Set and TDI Processed Observations

The ICON satellite, launched in October 2019, carries an ultraviolet imaging instrument that has a special Time Delay Integration (TDI) mode of operation, which was earmarked for studying low latitude far ultraviolet emission intensity distributions, especially the occurrence of EPB-s. In this paper we will discuss this special mode of operation and the data processing techniques used in studying the structure of the EIA and associated bubbles.

The ICON FUV instrument has two imaging channels (Mende et al. 2017). For the nighttime observations we use the short wave (SW) channel only and that is nominally centered at 135.6 nm. The detectors in each channel utilize an FUV image converter with a microchannel-plate (MCP) intensifier which is fiber-optically coupled to a CCD detector. The imaging channels are combined to share a common entrance aperture and optic axis which is pointed downward 20° from local horizontal and to the left (port side) direction. ICON is in a circular orbit at a nominal altitude of 600 km. See Fig. 1.

The 12-second integration time coupled with ICON's orbital motion of 7.6 km/s at spacecraft altitude causes a 91.2 km motional blur which becomes 87.5 km when projected on the 300 km altitude surface. By compensating for spacecraft motion using the TDI process we can greatly improve the spatial resolution performance of ICON FUV.

To compensate for the motion of the various regions in the image the object distance, the range distance to the emitting region from the spacecraft, is needed. In general this is an unknown variable and we need to assume a model for the geometry of the emitting object region. We assumed that there are two region and "Limb" and "Sub-limb" regions (Fig. 1). In the sub-limb region all the 135.6 nm emission is mapped to 300 km altitude. The "Sub-limb" region is a curved layer shown as PQ in Fig. 1 (also shown on Fig. 6) as the distance difference between the 300 km tangent height located at 1900 km from the satellite and the pierce point of the 300 km altitude surface at the bottom of the field of view 32 degrees below local horizontal which is located at 485 km distance from the satellite. This region PQ is 1425 km long as surface distance at 300 km altitude. Emissions that are produced at elevation angles higher than the view angle corresponding to the 300 km tangent height. They can be seen in Fig. 1 as region PR which is $1900 - 932 = 968$ km long surface distance at 300 km altitude and these images are referred to as "limb view" observations. The range distances for the limb view emissions pixels are calculated assuming to be originating at their own tangent heights.

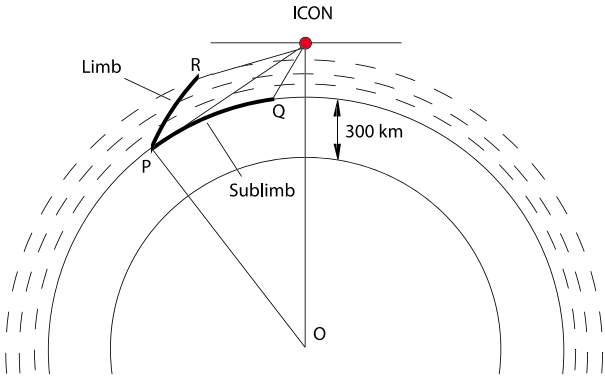

Fig. 1 The ICON satellite is traveling on its orbit illustrated as going into the page. The FUV instrument looks portside with the optic axis pointing 20 degrees down from the local horizontal. The diagram is not to scale. Assuming that the airglow tangent height is at 300 kilometer altitude the field of view can be split into a region (1) "Sub-limb" region illustrated as PQ where we projected all emissions to 300 km and (2) "Limb" region PR above 300 km tangent height where all emission regions were mapped to their respective tangent heights. The two regions are separated by the boundary line at P representing the limb tangent at 300 kilometers

It is not possible to employ a simple linear motion compensation scheme for correcting image blurring caused by satellite motion because of the range-to-target variance and pixels in the image do not drift uniformly across the detector. To accommodate the variable correction the image had to be first distorted before applying a simple uniform motion compensation. This was the basis of our novel digital real-time TDI image processing algorithm. To perform these transformations the FUV scene was split into the "Sub-limb" and "Limb" models. The algorithm performs image transformations on the incoming camera frames so that the resulting images are projected on to a distorted coordinate frame where the whole image travels uniformly as a result of the spacecraft motion. This distortion is the same as projecting the image on a spherical surface in the SOAP (Wilkins et al. 2017) coordinate system where the image moves uniformly on the surface. The resulting linear motion of the image is then compensated by progressively including an x or y address correction for the image displacement as the frames are recorded in memory on the spacecraft. This address correction corresponds to the net motion in the transformed-image space during a single image frame 0.125 s. In summary the TDI image processing involves the following steps:

(1) Transformation to remove geometric distortion of the optical system,
(2) Transformation to distort the frames to permit the linear correction for the objects' range variabillity to permit using uniform correction steps for all pixels. Note this transformation is equivalent to projecting the images back on to an imaginary curved surface at 300 km altitude for the "Sub-limb" view. For the "Limb view" the images were projected on the same 300 km surface but we used the geographic position of the tangent points of each ray. The transformations were accomplished using look up tables (LUT) on board the satellite. The LUT for steps 1 and 2 were combined into one single LUT.
(3) shifted to remove the image drift due to S/C motion.
(4) co-added 100 of corrected frames into a single image.

The resultant image was transmitted to ground in the S/C data downlink. The co-adding of images into a single image allowed the down linking of two dimensional images in spite of the data down link limitations.

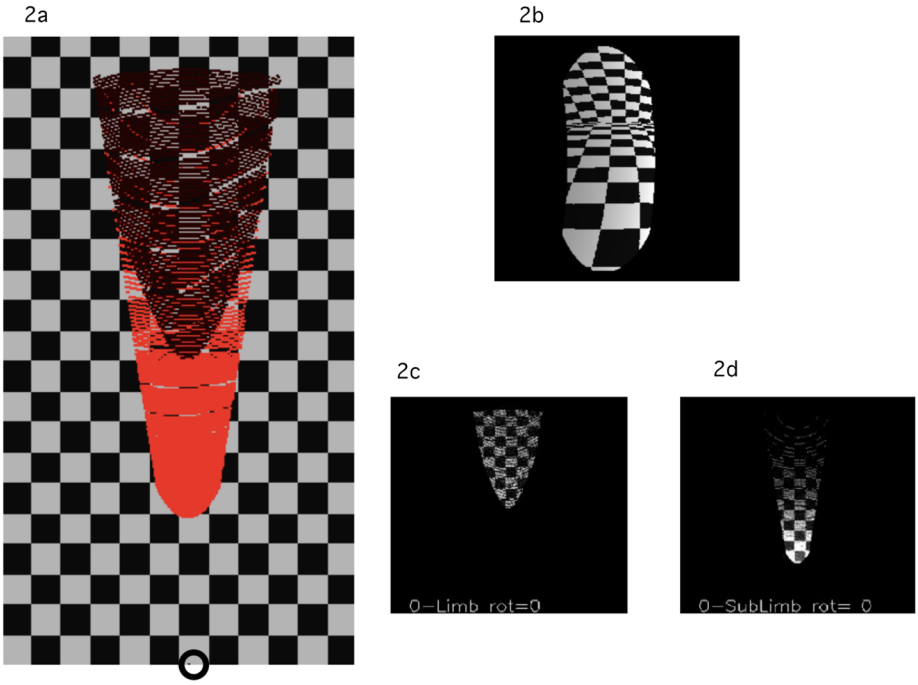

Fig. 2 a) Checker board image superposed on the 300 kilometer altitude surface in the SOAP coordinate system. The satellite is located at the ring shown at the bottom and is travelling in the "x" direction towards right. The view direction (*optic axis*) is pointing sideways in its normal "y" direction which is perpendicular to the satellite's velocity vector. b) Distorted image of the checker board as seen by icon FUV. c) Limb view image as projected on the 300 kilometer altitude surface with noise added. d) Sub-limb view image as projected on the 300 kilometer altitude surface with noise added

The whole system of the TDI process was modeled in software (Wilkins et al. 2017). The natural choice of coordinate transformation corresponding to both the nightside limb and sub-limb emission geometry and satellite motion is a map from the camera frame of reference into a spherical geographic system aligned with the orbit axis, referred to as Spacecraft Orbit-Aligned Position (SOAP) coordinates. SOAP coordinates are centered on Earth, where the x-direction is the spacecraft velocity direction, the z-direction is in the local vertical (zenith) and the y-is direction pointing north. SOAP latitudes and SOAP longitudes are computed using a spherical system with the satellite orbit plane as the equator recognizing that x and y are in the orbit plane. Figure 2a shows a projection of a checker board on the spherical surface at 300 km altitude. The spacecraft's field of view (24 degrees vertical and 18 degrees horizontal) is a projection on the 300 km altitude surface indicated with the limb view in black and the sub-limb in red. The ICON FUV optical system had a significant geometric distortion and the resultant distorted image is shown on Fig. 2b. The distortion correction was implemented by transforming the image with a lookup table which related the old pixel x and y values to the distortion corrected x' and y' values.

Because the orbit is almost circular, the ICON observatory moves at a nearly constant rate in the orbit-aligned SOAP longitudinal direction as the integration over time is performed. This fact is exploited so that image motion blur is corrected with an accumulating linear offset incremented for each incoming camera frame by an amount corresponding to the spacecraft's longitudinal displacement per frame. Figure 2a shows how the checkerboard

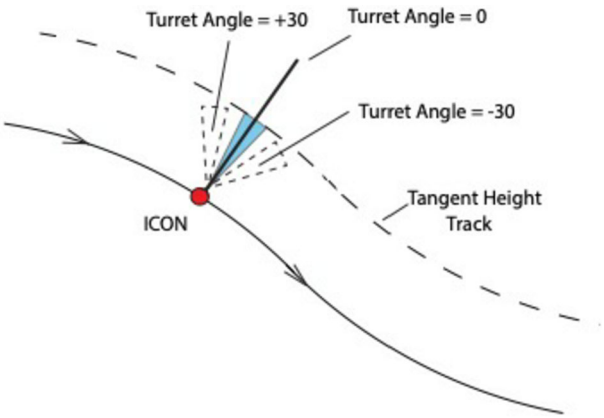

Fig. 3 Top view of the ICON satellite on its orbit (solid line) and the FUV look angles for turret angles 0, −30 and +30

that is drawn in longitude-latitude space is imaged by the upper limb and lower sub-limb images. The separator is the horizontal line at the limb tangent of the 300 km altitude region where the perspectives seems to depict the most distant observational range. Software simulation was completed by adding some Poissonian noise to the checkerboard pattern and co-adding 100 frames with the appropriate horizontal displacement simulating the output images as they would be co-added on board the moving S/C and applying the TDI motion compensation. The resultant images are shown in Fig. 2c and 2d.

The ICON FUV instrument's turret with the steering mirror can be rotated around a vertical axis ±30° in fixed steps to align the optic axis of the instrument close to the vertical plane containing the magnetic field and allow viewing the ionospheric plasma approximately parallel to the magnetic field. The viewing directions between turret angles between −30° and +30° are illustrated in Fig. 3.

When the turret angle is zero the FUV optic axis is in the plane perpendicular to the orbital velocity vector and FUV optic axis is directed "sideways" towards the left (port) side. During operations the turret angle is adjusted so that the FUV optics axis is looking closest to the vertical plane containing the magnetic field. Maximum angle the turret can be turned is 30 degrees forward (−30) or aft (+30). The magnetic field is calculated from an on board field model.

The software simulation included the turret rotations. An example is shown in Fig. 4 where we have included simulated images when the turret angle was 15° forward. The same checkerboard as in Fig. 2a was observed by the simulated instrument with the satellite moving from left to right except that the instrument field of view was rotated 15° degrees forward around the vertical axis of the satellite. One of the resultant distorted images seen by the instrument is shown in Fig. 4a. We have simulated the processing of 100 images with the checkerboard moving in the direction opposite to the satellite velocity and co-added the resulting images with the TDI offsets to produce a single limb and a single sub-limb image. The resultant images are presented as Fig. 4b and 4c. These images demonstrate that we can recover the resolution which would be lost otherwise with image blurring during the full 12 second exposures. The turret and steering mirror could rotate the optic axis over a ±30° range with 5° steps to allow the pointing in the local magnetic meridian direction. The various look directions required a special look up table for each.

A set of images taken on board ICON are shown on Fig. 5.

The onboard processing software produces 12 sec integrated images (Fig. 5 right side) similar to the software simulation code (Figs. 2c and 2d).

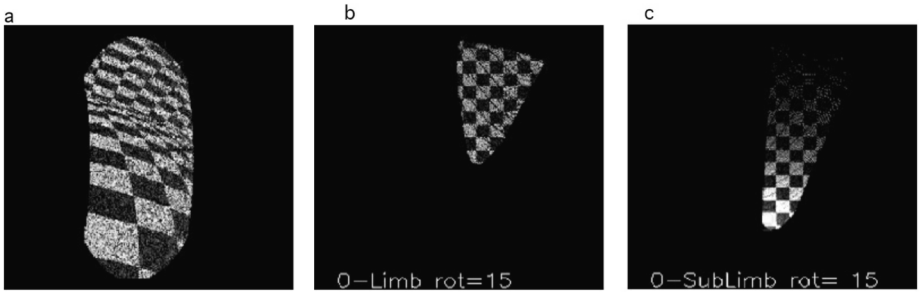

Fig. 4 a) Distorted image of the checkerboard as seen by icon FUV when the turret is pointing forward by 15 degrees. b) Limb view image as projected on the 300 kilometer altitude surface. c) Sub-limb view image as projected on the 300 kilometer altitude surface

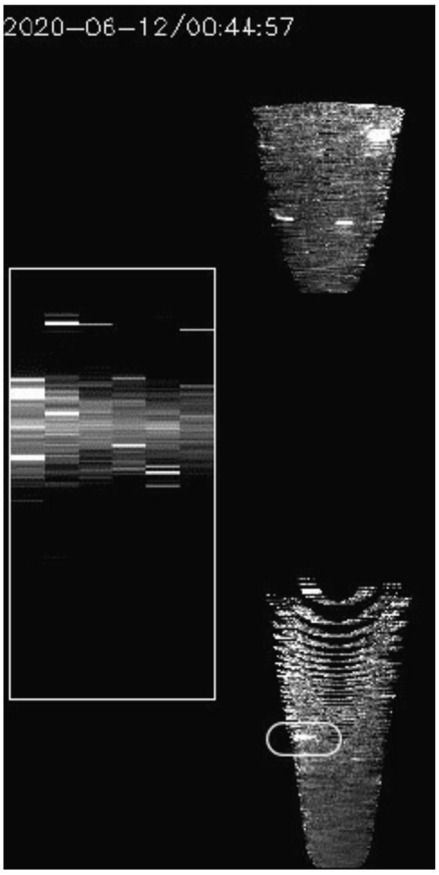

Fig. 5 Three types of ICON FUV data products from the short wavelength (SW) channel (Mende et al. 2017). Left side is the altitude profile data what is presented in the ICON data base consisting of six "stripes" or limb profiles with 3 degrees FOV width for each stripe. Right side upper "Limb TDI image" with 300 km tangent line at the top. Right side lower "Sub-limb TDI image". One star image is encircled

As discussed above the TDI system requires several geometric transformations of the images. One way to perform image transformations is the "forward process". This requires the knowledge of the functions $x_1 = f(x_0, y_0)$ and $y_1 = g(x_0, y_0)$ where x_0, y_0 are the original pixel coordinates, and x_1, y_1 are the new transformed coordinates. f and g are functions

or values from Look Up Table-s (LUT-s). This is the way we transform in the on-board flight system. The disadvantage of this forward process is that it leaves dark bands in regions where the image is being magnified and where some output pixels are spaced further apart leaving empty pixels in between in an otherwise luminous region. This effect can be seen on Fig. 5 especially in the lower sub-limb image where we find circular fringe like regions which are completely black. The simulation code which was used to generate Figs. 2 and 4 used backward projection process which automatically eliminated most of those black regions and produces fillers in regions where image magnification is taking place. It was recognized that it was more important to retain the quantitative intensity fidelity in the flight data and the aesthetics of the missing regions was less important whereas the artifacts created by the smoothing of the backward projection would be an undesirable feature. During the development of the flight system software the forward projection was used which leaves the data intact.

The final data product is processed on the ground and it consists of geographically mapped 135.6 nm data displays where the sub-limb images are co-added and superposed at the actual geographic location next to the ICON orbit. Each image is displaced with a stepwise offset of the 12 second travel time of the satellite or 87 km distance referred to a 300 km altitude surface sphere. The process is illustrated schematically on Fig. 6, where we show left to right motion for each 12 sec image. ICON FUV has a FOV with horizontal width of 18 degrees which translates to 602 km at the 1900 km maximum range distance of the 300 km altitude tangent height. The TDI process with 100 frames per 12 sec integration should reduce the smear theoretically to $87/100 = 0.87$ km blur which is less than the 3.1 km pixel resolution of the instrument. At the maximum distance from the spacecraft of 602 km this arrangement allows co-adding about 7 frames resulting in images that are each displaced by 87 km from each other. The width of the images at the maximum distance from the satellite is 602 km and each point on the map was the superposition of 7 consecutive frames as the S/C flies over. Closest to the spacecraft the observed region is only 154 km wide and containing only 2 exposures displaced by 87 km. However in the regions closer to the S/C the airglow intensities are contiguous without any black regions between pixels. The signal is co-added and the number of frames co-added are counted to produce an average intensity. The resultant average intensity at each output map pixel is calculated and shown as the result of the complete process. The largest gaps occur where the images are the widest, near the 300 km limb tangent region where there are seven super-posed images. At the other end the contributions are fewer but there are no gaps and the images look continuous. The net result is that co-adding in making the mapped images appear to eliminate the black regions produced by the forward projection of the individual frames.

1.2 Resolution Calibration of the TDI Sub-Limb Imaging

There are no stationary UV point sources sitting at the appropriate altitude and range distance from the spacecraft which could act as a calibration target. We often see bright stars in the upper portion of the sub-limb image and all parts of the limb image. In the images shown on Fig. 5 (right) there are several bright horizontal stripes due to UV stars seen by the instrument. One of the stars is encircled on Fig. 5 lower, sub-limb image. The stars appear stretched horizontally because of two reasons: (1) the spacecraft is constantly rotating in inertial space once per orbit to maintain the constant local vertical local horizontal (LVLH) attitude which makes stars appear to move (2) the TDI algorithm attempts to compensate for spacecraft motion by assuming that the star is located at the pierce point of the 300 km altitude spherical surface. This is an over correction because the star is not located at that

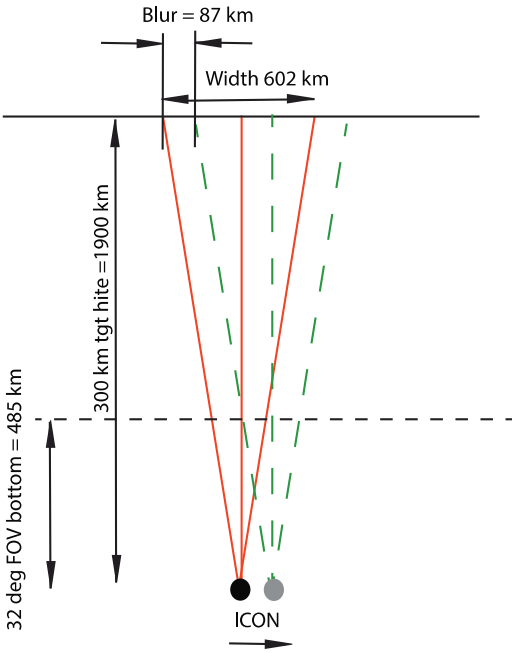

Fig. 6 Illustration of ICON sub-limb observation region near the 300 km altitude limb tangent. TDI imaging on board eliminates blurring due to the image motion compensation during the 12 sec exposures and produces blur free images 87 km apart. Each imaging region is in the 18 degree (600 km) horizontal FOV at the top of the diagram and it is a superpostion of 6 exposures

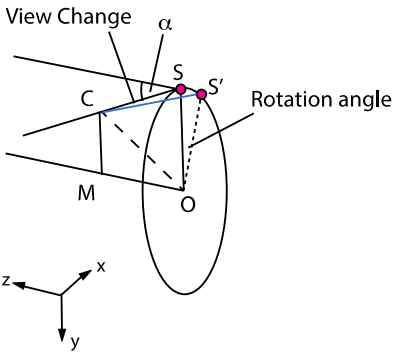

Fig. 7 Illustrations of star calibration of the TDI function on obit. Satellite at S viewing a point C which is on the 300 km altitude spherical surface located at an angle, a below the local horizontal at the satellite. Vector CS is the view direction from S to C at the start of the exposure. 12 seconds later S rotated to S' and the new vector for viewing C is the blue vector, CS'. The TDI system is designed to compensate for the view changing from vector CS to CS'

point. First we calculate the angular change represented by the streak. Then we calculate the needed TDI correction for the location of the star streak based on the circular orbital motion of the satellite. Following that we calculate the angular motion of the star due to the satellite rotation.

We used the Sub-limb image shown in Fig. 5 bottom right with the smeared star image shown circled. The width of the image was 53 pixels at the vertical location of the star image. The field of view of the imager was 18 degrees. The smear due to the star was 12 pixels corresponding to an angular shift of 4.07 degrees using a linearized calculation.

The TDI requirement was calculated by using a simple model of a vector pointing to C, which was located approximately at a = 19 degrees below local horizontal at the satellite. This is where the star image appeared to be located (Fig. 7). The vector CS is shown pointing to the satellite from there. During a 12 second exposure ICON proceeds forward on its orbit, which was simulated by rotating the ICON's position vector around the z axis while keeping the star point C fixed. The resultant new vector showed a 4.71°change in direction. Using the length of the vector between the satellite and the point representing the star this angle change represented a distance change of 87 km projected on the 300 km altitude surface.

We should recognize that a star would have a rotational smear even if no TDI correction were applied. During the 20 second exposure the S/C pitches 0.72° degrees and the star would generate a smear due to this attitude change due to orbital motion. We used the same rotation model (Fig. 7) but this time we rotated only the view vector alone, which is the reverse of the rotation of keeping the view vector to the star fixed and rotated the satellite around the z axis on its orbit. The results of the rotation in pitch showed that the change in the view vector direction was close to 0.72 degrees. Note that the 4.71° angular shift of the TDI overcompensated the rotational motion of the star which was only 0.72° degrees. The smear should have been about 4.71 – 0.72 ∼ 4.0 degrees. As explained above the actual measured smear of the star image was 4.1 degrees which is well within the errors in this calculation. In summary the TDI system seems to be performing as per plan and the ICON TDI System should have the ability to resolve objects of size of 10 km or less.

1.3 Nighttime Ionospheric Variability

In the subsequent discussions we will categorize the observed orbit displays into five categories:

1) Background only, no evidence of UV airglow and the entire orbit map plot is at background level.
2) Diffuse glow with only minimal fine scale structuring.
3) Continuous glow with limited number of field aligned stripes. In this category we see only a few reduced intensity magnetic field aligned stripes cutting across the glow.
4) Glow with intense but not field aligned structuring,
5) Regularly spaced with parallel field aligned structuring EPB-s.

Examples of these various categories are presented in Fig. 8.

1.4 The ICON TDI Data Products

A typical sub-limb ICON FUV TDI data product is shown in Fig. 9. Each panel represents one night pass of the ICON satellite. The Mercator map grid is 15 degrees in the latitude and longitude directions. The dash-dot-dot curve represents the magnetic dip equator. The mainly blue color coded region is the extent of the coverage of the ICON FUV instrument sub-limb view, which is looking downward from minus 32 degrees elevation angle up to ∼ −16° at the 300 kilometer tangent height. The position of the ICON satellite is represented by a row of dots seen underneath the color coded region. Each orbit data product is labeled with the start time and end time of the pass on the right top corner. The metadata consisting of latitude and longitude of the spacecraft, the turret angle, the solar local time of the observation, the high voltage and the gain applied to the display is presented on the left top of the figure. These metadata apply only to the UT time at the end of the pass which is shown on the top right corner.

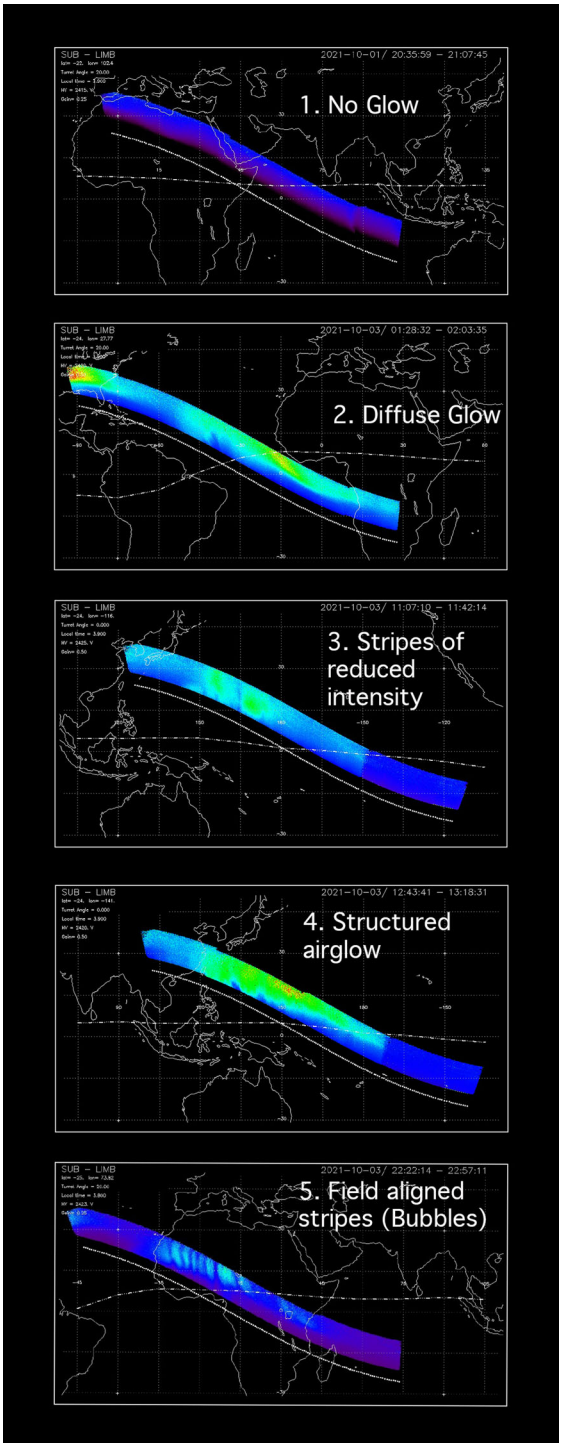

Fig. 8 Example of the categorization of the various orbit types as seen in the sub-limb TDI presentation

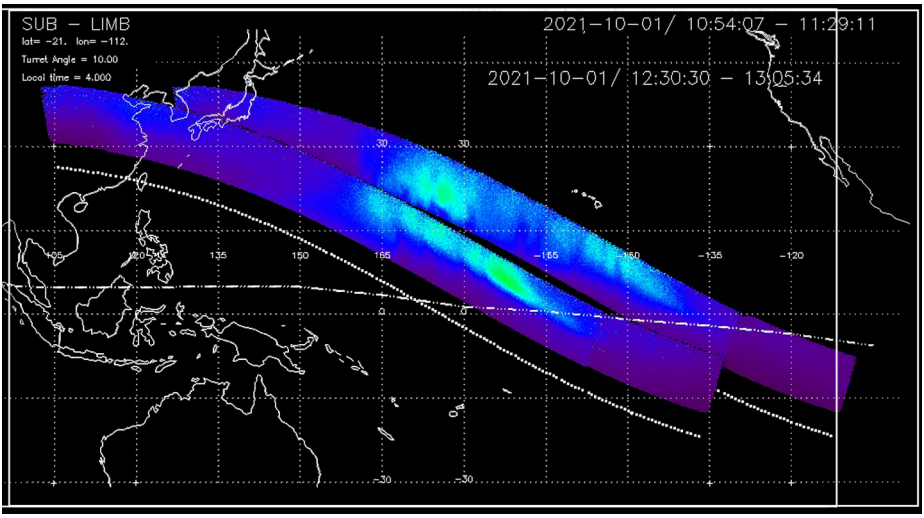

Fig. 9 The SW channel TDI sub-limb data shown for two consecutive orbits. Sublimb_full_TDI_map_2021-10-01 from 10:54 to 11:29 for the first orbit and the following superposed orbit taken from 12:30 to 13:05. The second orbit shows the westward adjacent region 90 minutes later

On Fig. 9 we show mapped images to demonstrate the relative location of the data product from two consecutive orbits. The first mapped image 10:54-11:29 is poleward and eastward of the magnetic equator and it is highly structured with distinct magnetically North-South features of reduced intensity. The image taken during the next orbit from 12:30 UT to 13:05 UT has less distinct structuring but also has some regions where darker patches separate the brighter diffuse emissions in the image.

There are significant difference between the two passes. As we can see the two passes map different geographic locations and there is a 96 minute time interval between the two orbits. The dynamics and variability of the EIA is discussed in the introduction and significant developments could easily occur on time scales of 96 minutes (e.g. Basu et al. 2009). Ionospheric bubbles typically propagate eastward and during the 96 minute orbital period, the bubbles would have moved several degrees eastward (to the right). The earlier orbit is the one on the right and slightly above. The location of the consecutive orbit tracks is unfavorable for tracking eastward motions. Nevertheless, the higher latitude and more western part of the two superimposed images show some north south continuity. A case could be made that the stripes have moved left (westward) from the top (earlier) image to the bottom.

1.5 Observations of the Equatorial Ionospheric Anomaly (EIA) by ICON

We normally expect to see the brightest low latitude glow in the EIA at about ± 15 degrees of magnetic latitude and a somewhat less intense band in between at the equator (Basu et al. 2009). In Figs. 10a and 10b we present the mapped emissions for 8 consecutive orbits taken on October the 9th, 2021. The displays were adjusted so that the longitudes of the orbit maps line up in the figures. ICON FUV does not have wide enough spatial coverage to see both peaks of the anomaly simultaneously, however the satellite observes each band individually as it flies through the region on each orbit. This presentation shows how much the ionospheric emissions change from one orbit to the next. The presence of the EIA is

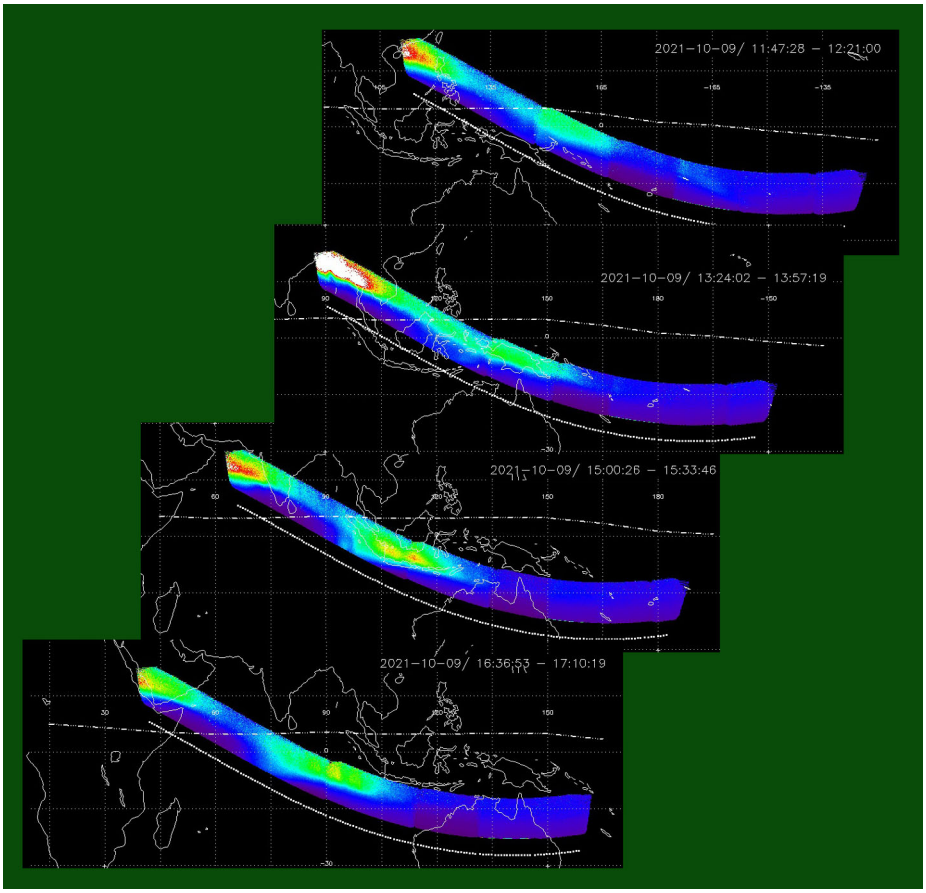

Fig. 10a Consecutive orbits. The EIA-is visible both south and north of the magnetic equator

well demonstrated on most orbits because there is a depression of intensity at the magnetic equator and brighter emissions are seen peaking some latitude distance from the equator.

The images also show that most of the plasma bubbles appear within 1 hour after sunset which is consistent with Tsunoda's hypothesis (Tsunoda 1985).

2 Direct Comparison with GOLD

The GOLD instrument (Eastes et al. 2019) is a spectrometer on a synchronous orbit satellite staring at the same atmospheric oxygen feature as ICON FUV.

The GOLD instrument is located so that it views most of South America, the Atlantic Ocean and a small part of Africa. Although GOLD's longitude coverage is limited it can provide information about the temporal variability of the emissions. ICON provides wide longitude coverage but only a single snapshot image during each overpass. In this way the two data sets are complementary.

Although ICON traverses the GOLD FOV region regularly there is very little simultaneous data taken with both ICON FUV and GOLD. This is because the ICON FUV instrument

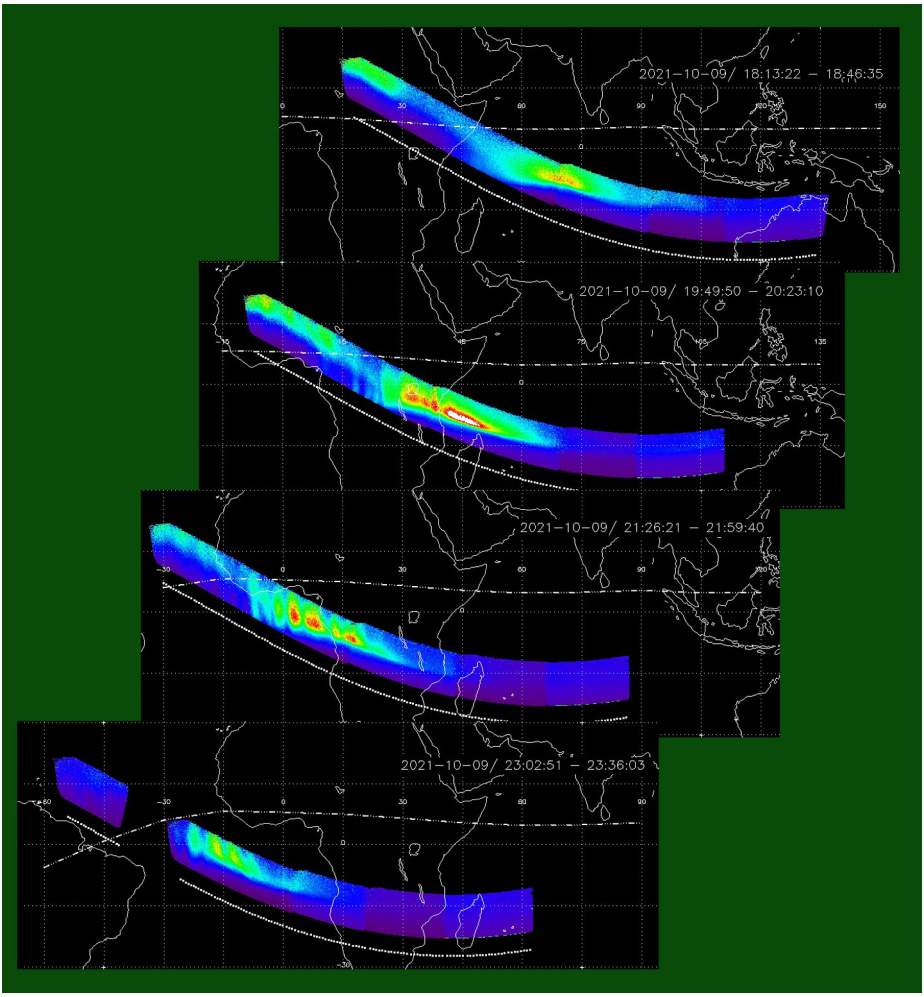

Fig. 10b Substantial structuring is visible in the EIA bands

is turned off in the South Atlantic Anomaly (SAA). In this region the Earth's radiation belts produce an intense downward flux of high energy particles that can potentially damage the ICON FUV instrument flight hardware if high voltage is being applied to the MCPs. As a precautionary measure the ICON FUV high voltage is switched off when it is passing the SAA. Unfortunately it is the same region where GOLD observes the ionosphere and ICON FUV coordinated observations with GOLD were only possible at the edge of the GOLD field of view.

The ICON FUV instrument steering mirror in the turret was not operated routinely until August 2021 and we expected a considerable improvement in resolving field aligned EPB-s after that date.

In Fig. 11 we show simultaneous data taken with ICON FUV and GOLD. The ICON satellite was just emerging from an SAA pass above the Eastern Atlantic Ocean. The inset shows the GOLD image and underneath a detail of the ICON FUV TDI image. The

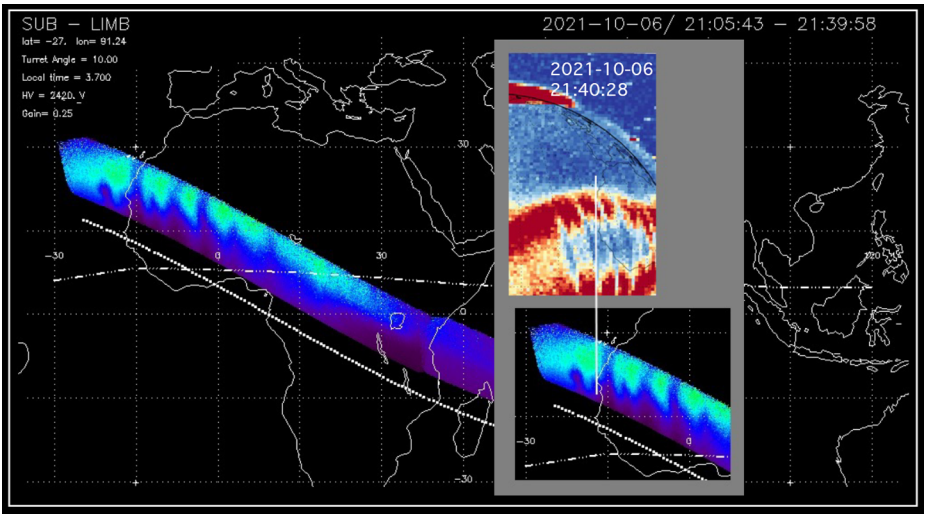

Fig. 11 Joint observations with ICON and GOLD on 2021-10-06. The ICON orbit entry and exit times for the pass are 21:05 and 21:39. The GOLD image was labelled that it was taken one minute after the ICON pass at 21:40. Note that ICON passed the region few minutes after 21:05. In the inset we have lined up the westernmost tip of Africa to help recognizing various features

horizontal positions of the images were lined up so that the map contour representing the westernmost point on the outline of Africa were horizontally lined up in both presentations. This match is indicated with a vertical white line. ICON imaged the northern branch of the EIA and the southern branch seen on GOLD, was outside of ICON's FOV. There is a large difference in the perspective of viewing between the two instruments. The view from GOLD is from a location westward in longitude of the observed region and some of the horizontal separation between the EPB-s are likely to be obscured by the altitude extent of the features. This could be the reason why the ICON TDI image shows much clearer separation of the EPB-s. GOLD's high-altitude vantage point is a long way west of this. ICON FUV is observing the region sideways somewhat parallel to the field aligned emission features from an altitude, which is less than 300 km above the emitting layer.

Another case of joint observations is shown in Fig. 12 one ICON orbit later starting at 22:42 and ending at 23:16. The GOLD image was taken at 22:40 UT about 10 minutes before the night side of the ICON orbit started. The rectangular frames were drawn to approximately bracket the −35 to 0 degrees longitude and the 0 to 30 degrees latitude region. Three of the most prominent bubbles can be recognized in both images.

Figure 13 presents another case of joint observations one day later starting at 22:48 and ending at 23:22. The GOLD image label shows that it was taken at 22:40 UT about 8 minutes before the night side orbit started. The rectangular frames were drawn to approximately bracket the −45 to −30 longitude and the 0 to 30 latitude regions. Three of the most prominent bubbles can be recognized in both images.

We have presented the GOLD and ICON FUV images side by side to show that the two instruments resolve similar structures and therefore we can make valid comparisons between the two data sets. The two data sets complement each other, GOLD is observing the nighttime features from a stable geographic location and the ICON FUV from a platform rapidly moving in geographic longitudes.

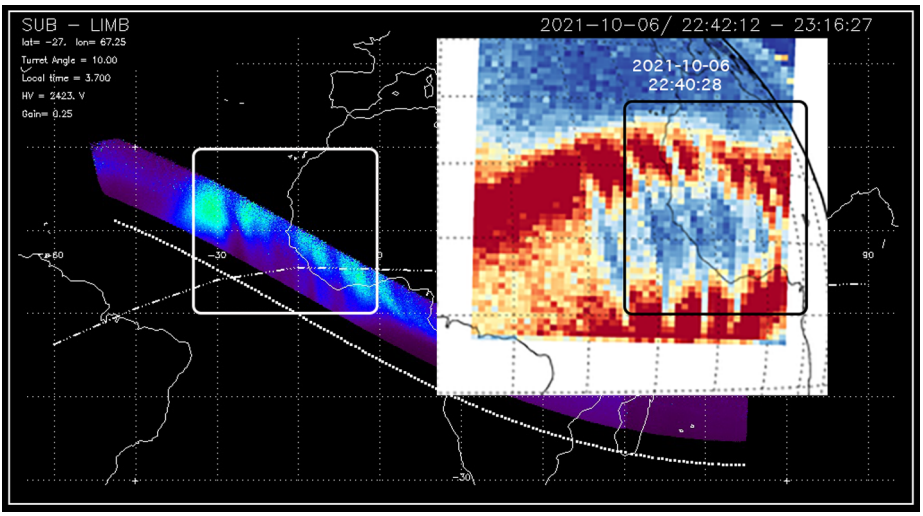

Fig. 12 Conjunction between ICON and GOLD observations taken on the orbit following the one presented in Fig. 11

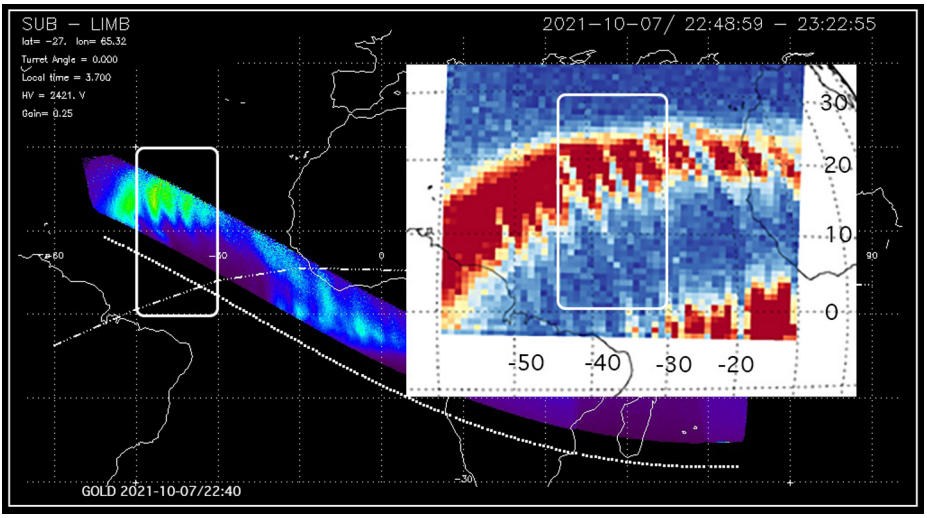

Fig. 13 ICON-GOLD image conjunction taken on 2021-10-07

In a prior section we discussed the categorization scheme of the night passes based on their morphological appearance. We used data that were available after the turret motion was implemented in August 2021. TDI sublimb plots were generated for every orbit for October, 1, 3, 6, 7, 9, 12, 15, 18, 21, 24, 27 and 30, 2021 with approximately 15 orbits each day amounting to a total of 179 orbits. The orbit plots were inspected, classified, and tabulated in terms of type in Table 1.

The ICON observations show that nighttime ionospheric emissions are present on 76% of the orbits demonstrating that ICON FUV is sufficiently sensitive to study the equatorial

Table 1 Frequency of occurrence of nightglow types from 179 orbits in October 2021

Type	Classification of nightglow during179 orbits	
1	Background only, no evidence of UV airglow	23.46%
2	Glow present but no fine scale structuring is seen	51.96%
3	Glow with limited number of field aligned stripes	6.15%
4	Some intense but not field aligned structuring,	7.82%
5	Regularly spaced parallel field aligned structured EPB-s	10.61%

FUV emissions. Categories 4 and 5, Structured airglow and regular field aligned striped structures, are seen on 18.4% of orbits.

It is important to note that the above percentages are stated in terms of 179 orbits that were surveyed. However FUV was turned off and did not observe for about 10% of the time because of the SAA crossing. Furthermore, the ICON FUV data is taken towards the northern limb tangent up to the 300 km altitude tangent point and depending on the turret angle that can be approximately 16 degrees northward of the satellite orbit track. ICON FUV covers a latitude region in the south that is greater in latitude than $-27^\circ + 16^\circ = -11^\circ$ and in the north that is less than $27^\circ + 16^\circ = 43^\circ$ geographic latitude. During magnetically quiet times we expect to see the EIA related emissions mostly between -15° and $+15^\circ$ geomagnetic latitude and we do not expect to see much bubble activity north of $+15^\circ$ magnetic latitudes. There is a region between $+15^\circ$ and $+43^\circ$ degrees geomagnetic where we typically do not expect substantial EIA type luminosities. We estimated that because of this consideration ICON spends only 48.3% of the observation time in regions where it could see the EIA features. Combining that with 90% coverage on account of the SAA we can only count on coverage 43.5% of the time.

It is reasonable to multiply the 179 orbit baseline by this factor before calculating the percentages of seeing structured glow. When ICON saw structured conditions (Category 4 and 5 orbits) 18.43% time. In summary if we only count ICON orbits when ICON was in the position to observe the equatorial latitude regions then the percentages should be increased by a factor of 1/.435 or 2.3 times and then the occurrence percentages should be increased to $18.43\% \times 2.31 = 37\%$.

Eastes et al. (2020) summarized the GOLD nighttime observations conducted for October and December 2018. These observations included all events where the presence of multiple similar structures was observable on the equatorward sides of the EIA at magnetic conjugate locations, even if it did not extend through the EIA, or a gap in the EIA on only one side of the equator. Eastes et al. (2020) reported that in 3 months of GOLD observations of uniform spacing of 3 or more depletions were identified on approximately one third of the nights ($\sim$34 out of 88 events). The spacing of the intensity depletions were generally quite regular but they varied from night to night. The bubbles ICON observed showed less regularity in spacing. Uniform spacing between bubbles was reported from ground-based imaging (Makela et al. 2010; Takahashi et al. 2015). Eastes et al. (2020) also reported that evenly spaced bubbles in the GOLD observations have limited extent, less than one hour of local time (15° longitude). This limitation of the local time and longitude of even spaced bubble sequences is also clearly seen in the ICON data.

Eastes et al. (2020) summarized the GOLD nighttime observations conducted between 1 October and 31 December 2018 and their occurrence rates are tabulated in Table 2 over three regions of their field of regards, South America, the Atlantic Ocean and Africa. ICON and GOLD quasi simultaneous bubble viewing occurred over Africa because of the SAA

Table 2 GOLD results reproduced from Eastes et al. (2020)

	South America	Atlantic Ocean	Africa
October 2018	73%	83%	51%
December 2018	54%	48%	17%

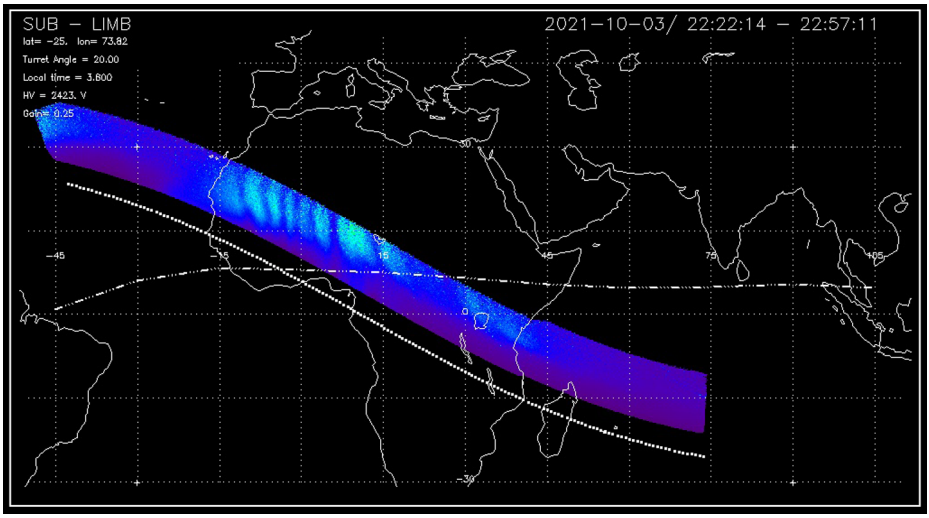

Fig. 14 Bubbles observed on the 2011-10-03 between 22:22:14 and 22:57:11 over Africa

avoidance of ICON. GOLD saw the least number of bubbles (51%) in this region in October 2018.

A relatively even spaced set of bubbles were observed on the 3rd of October on the night side of the orbit from 22:22 to 22:57 UT shown in Fig. 14. An enlargement of the bubbles is shown in Fig. 15a and 15b with a line indicating where the intensity profile of the emission was taken to be plotted in Fig. 15.

Our calibration of the images show that 15 degrees of latitude or longitude is equal to 90 pixels. Each pixel is equivalent to 0.166 degrees of latitude (2.9E-3 radians) great circle distance at 300 km altitude.

Two intensity plots were taken separated vertically by two rows of pixels (Fig. 15). We are interested in the horizontal resolution of the instrument and we want to disregard the uncorrelated pixel to pixel variation as noise. Having the two intensity profile we can look for correlated fluctuations between the two. The vertical dashed lines were added to line up with peaks in the upper plot. Note that very few of the high spatial frequency features line up with the peaks in the lower plot showing that these finer scale variations are mostly un-correlated. Clearly the large-scale fluctuations of peak separation of about 18-20 pixel bubble spacings are well correlated. These plots show that bubble spacing is properly resolved by the instrument but the higher spatial frequency fluctuations are not results of correlated imaging of vertically aligned features. The higher spatial frequency sharp peaks are random fluctuations probably associated with quantum or detector noise. They should not be included in bubble separation measurements. In summary we find the shortest properly resolved EPB spacing was 18 pixels or 3 degrees of latitude equivalent to about 350 km distance on the 300 km altitude surface.

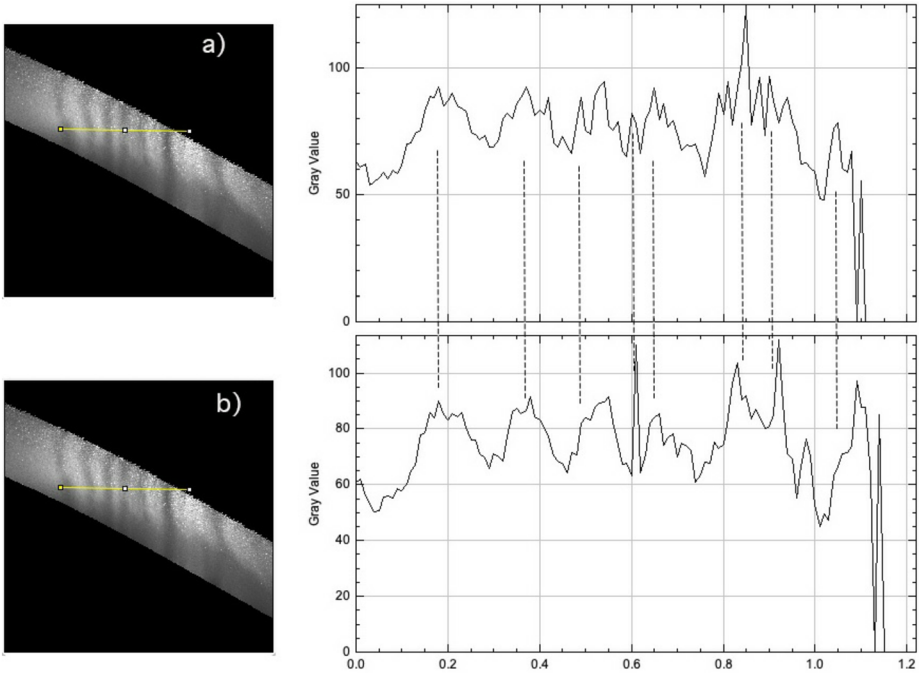

Fig. 15 The same data as in Fig. 13 presented without grid lines and maps. A yellow line indicates where the intensity plots were taken. The plots a) and b) are the same except that a) was taken 3 pixels above b). The corresponding intensity plots are shown on the right. The horizontal scale is in 100 pixels

3 Discussion and Summary

The ICON FUV imager was designed to make high resolution images of the nighttime near equatorial oxygen airglow emissions at 135.6 nm wavelength. To take these images the instrument had to take rapid exposures to minimize motional blurring of the image but at the same time it had to fit into the S/C restricted data volume and telemetry requirements. This was accomplished by using a novel Time Delay Integration (TDI) technique (Wilkins et al. 2017). The ICON FUV instrument views the Earth's limb airglow from above looking on the left side of the spacecraft, more specifically along the spacecraft −y axis when the spacecraft is in its normal local vertical local horizontal (LVLH) attitude where x is along velocity vector, z in the S/C nadir and y is to port (left side). Like in all TDI imagers (e.g. Mende et al. 2000) the camera takes rapid exposures which are shifted to compensate for the apparent motion of the image and then co-added to produce a single high signal to noise ratio image ready for transmission to the ground. On ICON this scheme of uniformly shifting of the whole image does not work because parts of the object have different object distances from the camera and they move with different apparent speeds on the image plane. To correct for this effect a special technique was developed. This arrangement requires that before co-adding, the images had to be transformed into a distorted frame in which the orbital motion is a singular constant vector for all pixels in the frame. Since we do not know the three dimensional distribution of the emitters we had to assume models for the 3D geometric distribution of the light sources. We used two models for the object distance for pixels, the "limb" and "sub-limb" models, which were used for the upper and lower parts

of the image, respectively. The technique was modeled to show that the scheme works in a computer simulation. This is the first report on the performance of the newly developed TDI system.

At the input of the instrument there was a turret with a flat mirror and a sun shade, which allowed steering the field of view so that the instrument could be looking in the plane of the local magnetic field at ICON. The TDI scheme resulted digitally co-adding 100 frames on board of the S/C to produce 12 sec integrated images which are down linked and re-assembled on the ground into maps of the O^+ emissions showing an entire ICON night pass. ICON with its relatively low inclination (27 degrees) orbit provides an extensive longitudinal coverage on each orbit. Prior UV imagers like GOLD (Eastes et al. 2019) provide comprehensive two dimensional time dependent images. GOLD is limited by being tied to a single geographic location. TIMED GUVI was on a high inclination orbit changing local time relatively slowly and missing a great deal of the equatorward low latitude regions at the wrong local times.

The ICON O^+ emission maps often show the presence of the Equatorial Ionospheric Anomaly (EIA) and show its structuring during 18.4% of the orbits. ICON was in the right position to see the EIA and the EPB-s only between $-15°$ and $+15°$ latitude only part of the time and ICON also lost 10% of its observation being inside of the SAA. If ICON had been on an orbit where it could make EIA region observations all the time then the count would be 2.3 times higher = 37%. Even then GOLD observed EPB structuring 51% of the time in October 2018. GOLD observed regular structuring in the form of (EPB-s) from its fixed West Atlantic longitude location more often than ICON. This poses three questions:

(1) Is the region where GOLD observes more prolific in EPB production than the global average in longitude that ICON may be seeing?
(2) Is it possible that the ICON observations are missing a fraction of EPB-s?
(3) Is it possible that October 2018 when GOLD observed the EPB-s was much more productive of EPB-s than October 2021 when ICON observed EPB-s?

ICON FUV should have resolution of the order of 10 km or better because of the TDI correction. The ICON FUV TDI was validated on orbit by using star images. When the TDI is switched off, when we take engineering mode image data, the stars look well defined sharp round images. In the TDI mode the star images are elongated in the direction of the orbital motion. This elongation takes place because the TDI processor tries to compensate the motion of the airglow region where the star is located and assumes the wrong object distance for the star. We measured the elongation and showed that it is consistent with difference between the shifting of the image by the TDI processor at the star's positon and the apparent motion of the star image on account of the S/C orbital rotation.

From the 179 orbits the highest resolution EPB-s in the ICON data were analyzed, and the shortest repetition rate bubbles were found to be 350 km from peak to peak. As we have seen from our comparison with GOLD the ICON resolved EPB-s appear to have similar dimensions to GOLD. The 350 km spacing is in very good agreement with many other authors (Makela et al. 2010; Makela and Otsuka 2012; Röttger 1973; Singh et al. 1997; Takahashi et al. 2009; Tsunoda and White 1981, Hysell and Chau 2006). Das et al. (2021) find that wave-like variations with horizontal wavelengths of 200–660 km are observed prior to sunset and these have a close connection with EPB spacings.

From comparisons of GUVI 135.6 nm disk data and ground based 777.4 nm imaging a consistent picture shows much finer scale dark structuring than what ICON FUV sees in the EIA (e.g. Fig. 1 of Kelley et al. 2003). These features do not appear to be magnetic field aligned plasma enhancements but very finely structured and mostly curved C shaped

depletions. Although ICON FUV may have the intrinsic resolution to see such size objects, ICON could not see the narrow curved structures while viewing horizontally and nearly parallel to the B field from low altitudes.

Although the spatial frequencies of EPB-s seen by ICON are much lower than those seen by Kelley et al. (2003) in the TIMED GUVI data, there is evidence for the "C" shapes seen by them. We refer to the eastward curving of north-south directed bubbles at higher latitudes, for example in the images of Fig. 15.

TIMED GUVI data was used in several studies of EPB-s for example Henderson et al. (2005a, 2005b) developed a method of automatic EPB identification in the disk images and statistically analyzed the EPB distribution. However TIMED with its high orbit inclination is less suited to do climatology of EPB-s. ICON on the other hand has rapid precession covering all local times at all latitudes in less than 30 days. The ICON observations will provide the database to investigate the special role of the alignment of the solar terminator and B field influencing the Rayleigh Taylor Instability (RTI) growth rate (Martinis et al. 2021).

In this paper we demonstrated that the ICON FUV TDI images are useful tools to investigate the near equatorial ionosphere. Soon we will have a whole year's data with the turret motion implemented which will provide a rich data set to look at the seasonal climatology of the low latitude nighttime ionosphere including EPB-s.

Acknowledgements The authors are thankful for the efforts of the broader ICON engineering and science teams. ICON is supported by NASA's Explorers Program through contracts NNG12FA45C and NNG12FA42I. ICON data can be retrieved from the Space Physics Data Facility (https://spdf.gsfc.nasa.gov/) or the ICON website (https://icon.ssl.berkeley.edu/Data).

Declarations

Competing Interests The authors declare no competing interests.

References

Appleton EV (1946) Two anomalies in the ionosphere. Nature 157(3995):691. https://doi.org/10.1038/157691a0

Balsley BB, Haerendel G, Greenwald RA (1972) Equatorial spread F: recent observations and a new interpretation. J Geophys Res 77:5625–5628. https://doi.org/10.1029/JA0771028p05625

Basu S et al (1996) Scintillations, plasma drifts, and neutral winds in the equatorial ionosphere after sunset. J Geophys Res 101(A12):26,795–26,809. https://doi.org/10.1029/96JA00760

Basu S, Basu S, Huba J, Krall J, McDonald SE, Makela JJ, Miller ES, Ray S, Groves K (2009) Day-to-day variability of the equatorial ionization anomaly and scintillations at dusk observed by GUVI and modeling by SAMI3. J Geophys Res 114:A04302. https://doi.org/10.1029/2008JA013899

Cai X, Burns AG, Wang W, Coster A, Qian L, Liu J et al (2020) Comparison of GOLD nighttime measurements with total electron content: preliminary results. J Geophys Res Space Phys 125:e2019JA027767. https://doi.org/10.1029/2019JA027767

Das SK, Patra AK, Niranjan K (2021) On the assessment of day-to-day occurrence of equatorial plasma bubble. J Geophys Res Space Phys 126:e2021JA029129. https://doi.org/10.1029/2021JA029129

Eastes RW, Solomon SC, Daniell RE, Anderson DN, Burns AG, England SL et al (2019) Global-scale observations of the equatorial ionization anomaly. Geophys Res Lett 46:9318–9326. https://doi.org/10.1029/2019GL084199

Eastes RW, McClintock WE, Burns AG, Anderson DN, Andersson L, Aryal S et al (2020) Initial observations by the GOLD mission. J Geophys Res Space Phys 125:e2020JA027823. https://doi.org/10.1029/2020JA027823

Eccles J (1998) Modeling investigation of the evening prereversal enhance- ment of the zonal electric field in the equatorial ionosphere. J Geophys Res 103(A11):26,709–26,719. https://doi.org/10.1029/98JA02656

Farley D, Bonelli E, Fejer B, Larsen M (1986) The prereversal enhancement of the zonal electric field in the equatorial ionosphere 11 of 12J. J Geophys Res 91(A12):13,723–13,728. https://doi.org/10.1029/JA091iA12p13723

Fejer B, Scherliess L, de Paula E (1999) Effects of the vertical plasma drift velocity on the generation and evolution of equatorial spread F. J Geophys Res 104(A9):19,859–19,869. https://doi.org/10.1029/1999JA900271

Haerendel G (1974) Theory of equatorial spread F. Max Planck Inst Für Phys and Astrophys, Garching, West Germany

Hanson WB, Moffett RJ (1966) Ionization transport effects in the equatorial F-region. J Geophys Res 71:5559–5572. https://doi.org/10.1029/JZ071i023p05559

Henderson SB, Swensen CM, Gunther JH, Christensen AB, Paxton LJ (2005a) Method for characterization of the equatorial anomaly using image subspace analysis of Global Ultraviolet Imager data. J Geophys Res 110:A08308. https://doi.org/10.1029/2004JA010830

Henderson SB, Swenson CM, Christensen AB, Paxton LJ (2005b) Morphology of the equatorial anomaly and equatorial plasma bubbles using image subspace analysis of Global Ultraviolet Imager data. J Geophys Res 110:A11306. https://doi.org/10.1029/2005JA011080

Hicks GT, Chubb TA (1970) Equatorial aurora/airglow in the far ultraviolet. J Geophys Res 75:6233. https://doi.org/10.1029/JA075i031p06233

Hysell DL, Chau JL (2006) Optimal aperture synthesis radar imaging. Radio Sci 41:RS2003. https://doi.org/10.1029/2005RS003383

Immel TJ, Sagawa E, England SL, Henderson SB, Hagan ME, Mende SB et al (2006) Control of equatorial ionospheric morphology by atmospheric tides. Geophys Res Lett 33:L15108. https://doi.org/10.1029/2006GL026161

Immel TJ, England SL, Zhang X, Forbes JM, DeMajistre R (2009) Upward propagating tidal effects across the E- and F-regions of the ionosphere. Earth Planets Space 61(4):505–512. https://doi.org/10.1186/BF03353167

Kelley MC, Larsen MF, Lahoz C, McClure JP (1981) Gravity wave initiation of equatorial spread F: a case study. J Geophys Res 86(A11):9087–9100. https://doi.org/10.1029/JA086iA11p09087

Kelley MC, Makela JJ, Paxton LJ, Kamalabadi F, Comberiate JM, Kil H (2003) The first coordinated ground- and space-based optical observations of equatorial plasma bubbles. Geophys Res Lett 30(14):1766. https://doi.org/10.1029/2003GL017301.

Lühr H, Häusler K, Stolle C (2007) Longitudinal variation of F region electron density and thermospheric zonal wind caused by atmospheric tides. Geophys Res Lett 34(16):L16102. https://doi.org/10.1029/2007GL030639

Makela JJ, Otsuka Y (2012) Overview of nighttime ionospheric instabilities at low-and mid-latitudes: coupling aspects resulting instructuring at the mesoscale. Space Sci Rev 168(1–4):419–440. https://doi.org/10.1007/s11214-011-9816-6

Makela JJ, Vadas SL, Muryanto R, Duly T, Crowley G (2010) Periodic spacing between consecutive equatorial plasma bubbles. Geophys Res Lett 37:L14103. https://doi.org/10.1029/2010GL043968

Martinis C, Daniell R, Eastes R, Norrell J, Smith J, Klenzing J et al (2021) Longitudinal variation of post-sunset plasma depletions from the global-scale observations of the limb and disk (GOLD) mission. J Geophys Res Space Phys 126:e2020JA028510. https://doi.org/10.1029/2020JA028510

Mende S, Heetderks H, Frey H, Lampton M, Geller S, Abiad R, Siegmund O, Tremsin A, Spann J, Dougani H, Fuselier S, Magoncelli A, Bumala M, Murphree S, Trondsen T (2000) Space Sci Rev 91(1/2):271. https://doi.org/10.1023/a:1005227915363

Mende SB, Frey HU, Rider K et al (2017) The Far Ultra-Violet Imager on the Icon Mission. Space Sci Rev 212:655–696. https://doi.org/10.1007/s11214-017-0386-0

Ossakow SL (1981) Spread-F theories: a review. J Atmos Terr Phys 43:437–452. https://doi.org/10.1016/0021-9169(81)90107-0

Rishbeth H (1981) The F region dynamo. J Atmos Terr Phys 43:387–392. https://doi.org/10.1016/0021-9169(81)90102-1

Röttger J (1973) Wave-like structures of large-scale equatorial spread-F irregularities. J Atmos Sol-Terr Phys 35(6):1195–1206. https://doi.org/10.1016/0021-9169(73)90016-0

Singh S, Johnson FS, Power RA (1997) Gravity wave seeding of equatorial plasma bubbles. J Geophys Res 102(A4):7399–7410. https://doi.org/10.1029/96JA03998

Sultan PJ (1996) Linear theory and modeling of the Rayleigh-Taylor instability leading to the occurrence of equatorial spread F. J Geophys Res 101(A12):26875–26891. https://doi.org/10.1029/96JA0068

Takahashi H, Taylor MJ, Pautet P-D, Medeiros AF, Gobbi D, Wrasse CM et al (2009) Simultaneous observation of ionospheric plasma bubbles and mesospheric gravity waves during the SpreadFEx Campaign. Ann Geophys 27:1477–1487. https://doi.org/10.5194/angeo-27-1477-2009

Takahashi H, Wrasse CM, Otsuka Y, Ivo A, Gomes V, Paulino I et al (2015) Plasma bubble monitoring by TEC map and 630 nm airglow image. J Atmos Terr Phys 130–131:151–158. https://doi.org/10.1016/j.jastp.2015.06.003

Tsunoda RT (1985) Control of the seasonal and longitudinal occurrence of equatorial scintillations by the longitudinal gradient in integrated E region Pedersen conductivity. J Geophys Res 90(A1):447–456. https://doi.org/10.1029/JA090iA01p00447

Tsunoda RT, White BR (1981) On the generation and growth of equatorial backscatter plumes 1. Wave structure in the bottomside F layer. J Geophys Res 86:3610–3616. https://doi.org/10.1029/JA086iA05p03610

Wilkins CW, Mende SB, Frey HU, England SL (2017) Time-delay integration imaging with ICON's far-Ultraviolet Imager. Space Sci Rev 212:715. https://doi.org/10.1007/s11214-017-0410-4

Woodman RF, La Hoz C (1976) Radar observations of F region equatorial irregularities. J Geophys Res 81:5447–5466. https://doi.org/10.1029/JA081i031p05447

Authors and Affiliations

S.B. Mende[1] · H.U. Frey[1] · S.L. England[2] · T.J. Immel[1] · R.W. Eastes[3]

✉ S.B. Mende
mende@ssl.berkeley.edu

[1] Space Sciences Laboratory, University of California, Berkeley, CA, USA

[2] Virginia Polytechnic Institute, State University, Blacksburg, VA, USA

[3] Laboratory for Atmospheric and Space Physics, University of Colorado Boulder, Boulder, CO, USA